

Unwrapping Ground Displacement Signals in Satellite Radar Interferograms With Aid of GPS Data and MRF Regularization

Sverrir Gudmundsson, Jens Michael Carstensen, and Freysteinn Sigmundsson

Abstract—Synthetic aperture radar (SAR) images acquired by radar satellites at different times can be combined into interferograms that reveal information about the change in range from ground to satellite, wrapped into phase fringes corresponding to half the radar wavelength. We describe a methodology that uses Markov random field (MRF) regularization and simulated annealing optimization to unwrap such differential interferograms. Often, repeated global positioning system (GPS) geodetic measurements are available in an area covered by interferograms. Here, such repeated GPS observations are used to provide a complementary measurement of the unwrapped change in range at sparse locations. The process of unwrapping interferograms can be initialized and guided with such sparsely located “correct” values. Both interferograms and GPS observations may include several error factors, which are reduced before combining the two observations. GPS-measured range change is used to eliminate residual orbital error. In the unwrapping procedure, a vectorized lowpass filter is used to gain temporarily increased smoother variation of the phase. For the purposes of initializing the unwrapping process, virtual unwrapped interferograms are created by ordinary kriging of GPS-measured range change. The initial interferograms are then optimized further by using MRF regularization that incorporate the assumption of a smoothly varying displacement field and the relationship of the unwrapped images to the GPS observations. A simulated annealing optimization algorithm is used to find an optimal solution of the MRF regularization. The smoothed unwrapped interferograms are then used to construct unwrapped versions of the unfiltered input interferograms. Several additional image analyses methods are used in the optimization process to make the unwrapping more efficient and faster. The unwrapping technique is applied to unwrap interferograms from the Reykjanes Peninsula, in southwest Iceland.

Index Terms—Crustal deformation, global positioning system, Iceland, interferograms, remote sensing, Reykjanes Peninsula, satellite radar interferometry, unwrapping.

I. INTRODUCTION

INTERFEROMETRIC analysis of synthetic aperture radar (SAR) images and global positioning system (GPS) geodetic measurements provide two complementary views on the defor-

mation of the earth’s surface. SAR images acquired by radar satellites at different times (master and slave images) can be combined into interferograms that reveal the change in range from ground to satellite (the slant-range shift, $\Delta\rho$), expressed as interferometric fringes [1]. Each fringe corresponds to change in range of $\lambda/2$, where λ is the radar wavelength ($\lambda = 5.67$ cm for the ERS satellites). This assumes that fringes due to topography have been removed with usage of a digital elevation model (DEM) [2].

Repeated GPS measurements provide pointwise information on three-dimensional (3-D) movements at the occupied geodetic stations [3]. The projection of a 3-D GPS displacement vector, onto a unit vector from ground to a radar satellite, provides an independent local measure of range change. If GPS-derived displacements exist in an area covered by an interferogram, then these observations can be projected into slant-range shift, in order to create corresponding unwrapped pixel values in an interferogram at sparse locations corresponding to the GPS sites.

Several complementary methods have been created to unwrap interferograms [4]. Here, we present a methodology that uses GPS observations, Markov random field (MRF)-based regularization, and simulated annealing optimization [5], [6]. The MRF model uses assumptions about the smoothness of the displacement field and the relationship of the unwrapped interferograms to the GPS observations. Some error factors are eliminated from the wrapped interferograms before they are unwrapped. GPS observations can be used to eliminate residual orbital errors. A vectorized filtering [1], [7] is used within the unwrapping procedure to smooth and gain increased coherence of the wrapped interferograms. This greatly reduces degradation effects from noise errors and occurrence of phase gradient errors [4] and makes the MRF regularization more efficient. The process is initialized with virtual unwrapped interferograms created by interpolation of GPS measurements, and further optimization is conducted with MRF regularization and simulated annealing iteration. Finally, the smoothed and unwrapped interferogram is used to construct an unwrapped version of the nonsmoothed input interferogram. Thus, the unwrapped phase is congruent (the same) [4] with the wrapped phase of the input interferograms with orbital phase errors eliminated.

In an MRF regularization, an optimal image is interpreted as a realization of a random variable, where each pixel value in the image grid is only dependent on its nearest neighbors. This provides a convenient way of modeling image texture and spatial correlation of image pixels. Furthermore, simulated annealing and MRF regularization is a very suitable method to use

Manuscript received May 22, 2001; revised April 8, 2002. This work was supported by European Community Contract ENV4-CT97-0536+A6 to the PRENLAB-2 project and EVG1-CT-2001-00046 to the RETINA project, a special grant from the Icelandic government, and a grant from the Icelandic Research Council.

S. Gudmundsson is with the Science Institute, University of Iceland, Reykjavik 107, Iceland.

J. M. Carstensen is with the Technical University of Denmark, Lyngby DK-2800, Denmark

F. Sigmundsson is with the Nordic Volcanological Institute, Reykjavik 108, Iceland.

Publisher Item Identifier 10.1109/TGRS.2002.802516.

in image optimization, such as for image reconstruction. Results of applying the method to interferometric and GPS observations from the Reykjanes Peninsula, in southwest Iceland, are presented.

II. DESCRIPTION OF THE PROBLEM

The relationship between an unwrapped (\mathbf{i}_{Uw}) and a wrapped (\mathbf{i}_W) interferogram can be written as

$$\mathbf{i}_{Uw} = \mathbf{i}_W + \mathbf{n} \frac{\lambda}{2} \quad (1)$$

where \mathbf{n} is a circle number matrix (integer values), and λ is the wavelength of the SAR unit. Unwrapping of an interferogram can, therefore, be regarded as a problem of finding the circle number matrix \mathbf{n} in (1).

A phase change $\Delta\theta$ in each pixel of an interferogram can be due to a number of effects. It can be written as

$$\Delta\theta = \frac{2\pi}{\lambda} i_w = \Delta\theta_{\text{displacement}} + \Delta\theta_{\text{orbital}} + \Delta\theta_{\text{topography}} + \Delta\theta_{\text{noise}} \quad (2)$$

where $\Delta\theta_{\text{displacement}}$ is due to the surface displacement. A phase shift of $\Delta\theta$ from 0 to 2π corresponds to the scalar change in range of i_w from 0 to $\lambda/2$. Orbital and topographical errors can be reduced by using information about the orbital trajectories and the surface topography [1]. However, often, there are residual orbital and topographical errors. Interferograms may then also include several other noise factors ($\Delta\theta_{\text{noise}}$), such as tropospheric and ionospheric artifacts, as well as effects due to coherence degradation. If all error factors can be corrected for, then the scalar change in range from the satellite to ground can be described for each pixel by

$$\Delta\rho = \frac{\lambda}{2\pi} \Delta\theta_{\text{displacement}} = -\mathbf{u} \cdot \hat{\mathbf{s}}^T \quad (3)$$

where \mathbf{u} is the 3-D displacement vector, and $\hat{\mathbf{s}}$ is the unit vector pointing from the ground toward the satellite.

The relationship between sparse GPS observations of \mathbf{u} and the interferometric observations (i_w) of $\Delta\rho$ is expressed in (3). By using (3), the GPS observations can be mapped into the slant-range of the satellite. This gives a measure of unwrapped values of a range change in an interferogram at locations corresponding to the GPS points.

III. OBSERVATIONS

A. GPS and Interferometric Observations From the Reykjanes Peninsula, Iceland

As a test area for our procedure, we use the Reykjanes Peninsula, an obliquely spreading subaerial portion of the Mid-Atlantic Ridge in southwest Iceland (see Fig. 1). GPS measurements have been conducted at 38 sites on the peninsula, initially in 1993, and again in 1998 (see Fig. 1) [8], [9]. Of the 38 GPS observations, 37 were used for this work. Uncertainties of the GPS-measured east, north, and vertical 1993–1998 displacements have been estimated [9] on average as ± 2.6 mm, ± 3.2 mm, and ± 12.1 mm,

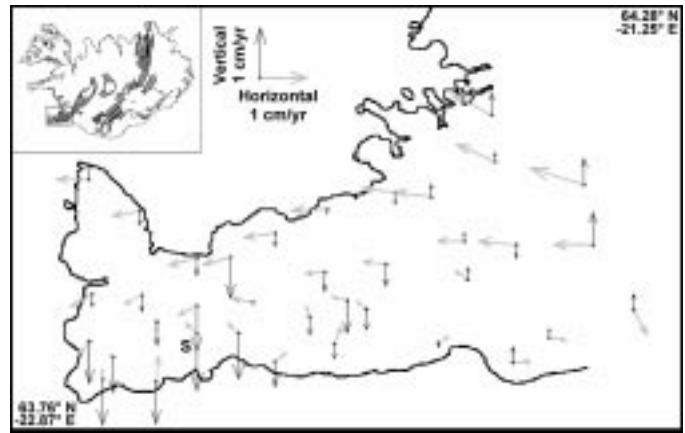


Fig. 1. Reykjanes Peninsula, southwest Iceland (the location is shown in the inset map of Iceland). Black and gray vectors show GPS-measured vertical and horizontal displacement rates, respectively, in the period from 1993 to 1998, displayed as annual averages (S: Svartsengi).

respectively (highest for the vertical component). Uncertainties of the vertical component were within ± 14.0 mm at 35 of the 37 GPS sites, but large vertical uncertainty of ± 16.5 and ± 21.0 mm were observed at two of the sites.

Four wrapped interferograms from the Reykjanes Peninsula were used for this study [see Table I and Fig. 2(a)–(d)], acquired with the two European ERS-1 and ERS-2 satellites, from descending satellite passes. They are the same as used in [10], in addition to one new [see Fig. 2(c)] formed in the same way as the others with the Centre National d’Etudes Spatiales (CNES)-developed DIAPASON software. For those interferograms, the unit vector in (3) is given as [10]

$$\hat{\mathbf{s}} \approx [0.34 \text{ E}, -0.095 \text{ N}, 0.935 \text{ V}] \quad (4)$$

where E, N, and V stand for east, north, and vertical, respectively. One fringe corresponds to a range change of $\lambda/2 = 2.835$ cm. Topographical effects have been eliminated by using a DEM, and known orbital effects have also been removed by using knowledge about the orbital trajectory. The interferograms may include residual errors, as explained in Section II.

Possible inconsistency has to be considered before combining the interferometric and GPS observations.

- 1) The contribution of the GPS observations to the slant-range shift [see (4)] is mainly through the vertical GPS component (the one with highest errors).
- 2) In some parts of the interferograms, tropospheric and ionospheric artifacts occur that typically generate smoothly varying features within the image area, e.g., “large” blob-like disturbances [7].
- 3) Our interferograms suggest some variable rate of deformation for some parts of the image areas. This can lead to some discrepancy, since the interferograms and the GPS measurements cover different elapsed time intervals. However, motion at the Reykjanes Peninsula in the 1992–1998 period can be assumed to be mostly smooth and steady (not time dependent). This is supported by the high consistency, in general, between the interferometric and GPS datasets and the fact that no large earthquakes were recorded there during the study period [8]–[10].

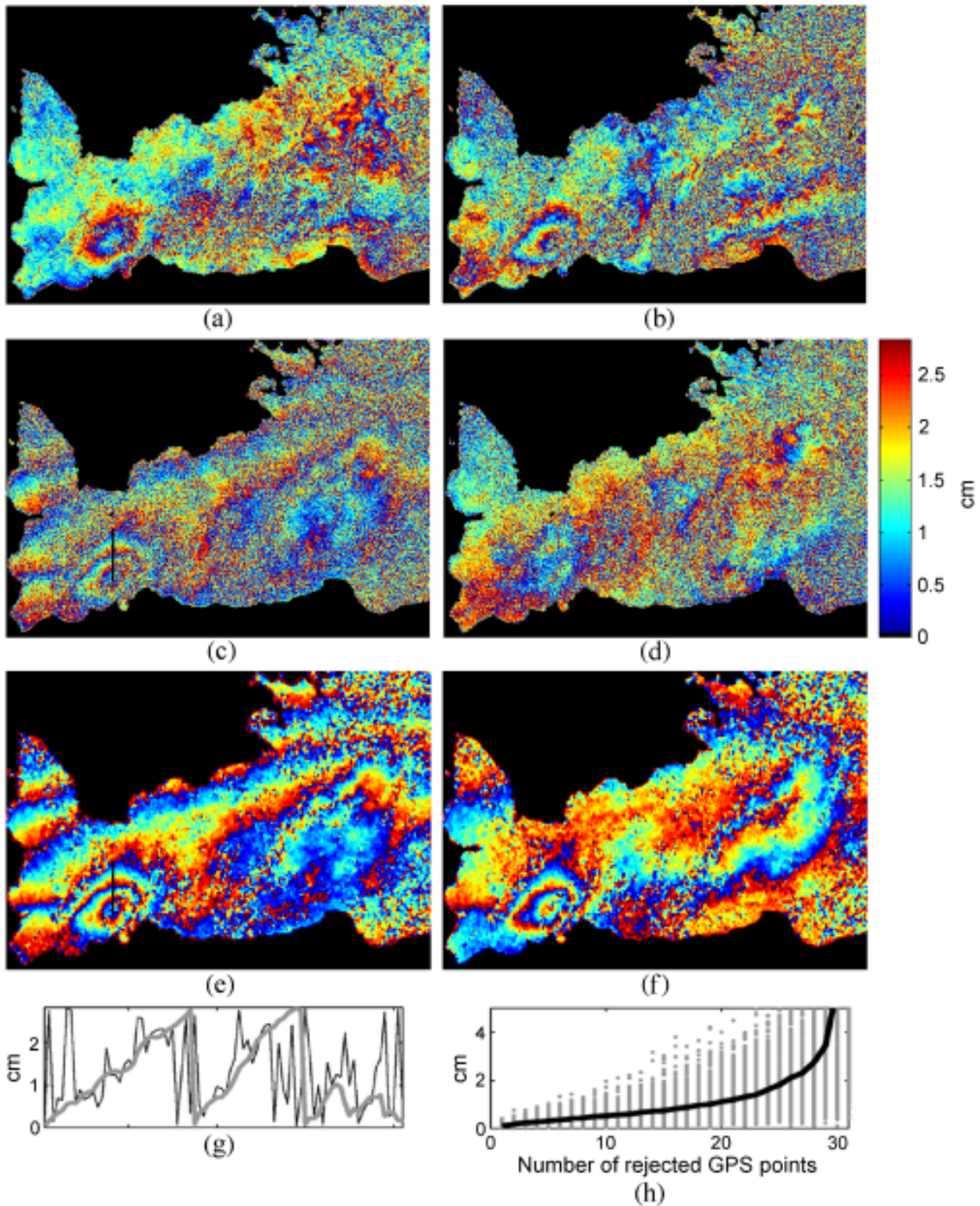


Fig. 2. Wrapped interferograms from the Reykjanes Peninsula. See Fig. 1 for location. (a)–(d) Interferograms listed in Table I. (e) Interferogram in (c) after vectorized filtering. (f) Interferogram in (e) after tilting with aid of the GPS observations. Three of the 37 GPS sites (Fig. 1) are located outside the area covered by the interferograms. Observations from these sites cannot be used for the tilting. The same colorbar applies to all the interferograms. (g) Profiles from (c) (black line) and (e) (gray line). The location of the profiles is shown with a black line in (c) and (e). (h) Maximum deviation between the residual phase plane used to tilt (e) (estimated using the 34 GPS observations located within the image areas) and residual phase planes estimated by randomly rejecting 1–31 of the 34 GPS points (gray scatter points). The black line shows the average deviation.

TABLE I
CHARACTERISTICS OF THE INTERFEROGRAMS. FIRST COLUMN REFERS TO THE NUMBERING IN FIGS. 2 AND 9

Number	Master orbit	Date of observation	Slave orbit	Date of observation	Elapsed time (years)	Altitude of ambiguity (m)
a	5565	08.08. '92	10575	24.07. '93	0.96	59.0
b	5565	08.08. '92	21941	25.09. '95	3.13	43.6
c	5565	08.08. '92	7278	09.10. '96	4.17	22000
d	10575	24.07. '93	21941	25.09. '95	2.17	166.0

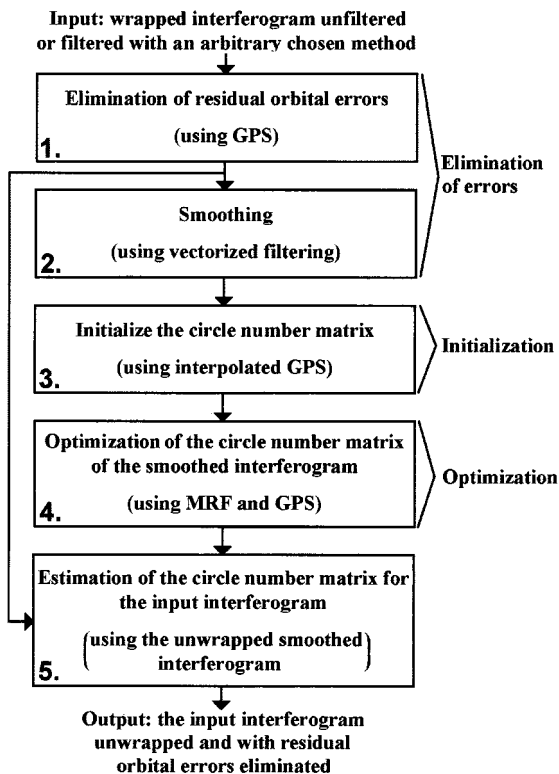


Fig. 3. Overview of the unwrapping process.

IV. OVERVIEW OF THE UNWRAPPING PROCESS

Fig. 3 shows a block diagram of the unwrapping process. Effects from some error factors are best reduced before unwrapping. GPS observations are used in Step 1 to compensate for residual orbital errors (systematic errors). A filter is exploited in Step 2 to reduce speckle noise (with high “spatial frequency”) e.g., due to decorrelation, and to increase the smoothness of the wrapped interferogram. The smoothing results in increased effectiveness of the optimization in Step 4. The unwrapping is initialized in Step 3 by using a virtual interferogram created from interpolated GPS observations. After optimization (Step 4), the smoothed and unwrapped interferogram is used in Step 5 to construct an unwrapped version of the nonsmoothed interferogram from Step 1. Methods behind each step in Fig. 3 are explained in more detail in Sections V–VII. In Section VIII, we will demonstrate the procedure further with an applied example.

In the process, the GPS observations are used for the following reasons:

- 1) reduce residual orbital errors (Step 1);
- 2) generate virtual interferogram for initialization (Step 3);
- 3) in the MRF model used in the optimization (Step 4).

It should be noted that tropospheric and ionospheric artifacts cannot be eliminated with the methods described in this paper.

V. ELIMINATION OF ERROR EFFECTS

A. Noise Reduction by Vectorized Filtering

The modulated characteristics of the interferograms need to be considered before filtering. Here, this is handled by using vectorized filtering [1], [7], [11]. Vectorized filtering can be interpreted as a filtering of the periodical phase changes in (2), projected into cosine and sinusoidal signals. The cosine and sinusoidal signals are filtered separately before projecting back. The filtered interferogram is given as

$$\mathbf{i}_f = \frac{\lambda}{2\pi} \angle(f * \mathbf{C}) \quad (5)$$

where

- f some linear filter coefficients (e.g., moving-average window);
- $*$ convolution;
- \angle angle.

\mathbf{C} is a complex intensity image given by

$$\begin{aligned} \mathbf{C} &= \exp\left(\frac{j \cdot 2\pi \cdot \mathbf{i}_W}{\frac{\lambda}{2}}\right) = \exp(j \cdot \Delta\theta) \\ &= \cos(\Delta\theta) + j \cdot \sin(\Delta\theta) \end{aligned} \quad (6)$$

where $\Delta\theta$ and \mathbf{i}_W are periodical within the interval $[0, 2\pi]$ and $[0, \lambda/2]$, respectively. The result of vectorized filtering the 4.17-year interferogram from the Reykjanes Peninsula [see Fig. 2(c)] with a $0.5 \text{ km} \times 0.5 \text{ km}$ moving-average window is shown in Fig. 2(e).

The vectorized filter is exploited to reduce error distortions and gain increased smoothness and coherence of the wrapped phase before optimization (Step 2 in Fig. 3). A simple moving-average window has proven to be very suitable for this purpose. It should be noted that the effects of oversmoothing narrow features and high-frequency information are not inherited in the unwrapped output interferogram due to Step 5 in the unwrapping process (Fig. 3). Furthermore, the input interferogram can either be unfiltered or filtered with arbitrary chosen method (Fig. 3), e.g., with a filter that tends to preserve narrow features.

B. Elimination of Residual Orbital Errors by GPS Observations

Residual orbital errors need to be eliminated from the wrapped interferograms before utilizing the GPS data in the unwrapping process. Here, we use the same method as in [11], assuming

that the deformation rate is steady and that the residual orbital errors can be described by a tilted plane and an offset (a phase plane). Due to the assumption of steady deformation, the observed GPS motion vectors can be scaled to fit the elapsed time interval of the interferogram. The scaling is given as $(t_{\text{SAR}_1-\text{SAR}_2})/(t_{\text{GPS}_1-\text{GPS}_2})$, where $(t_{\text{SAR}_1-\text{SAR}_2})$ and $(t_{\text{GPS}_1-\text{GPS}_2})$ are the elapsed time intervals of the interferometric and GPS observations, respectively. The scaled GPS observations are then used to provide an unwrapped measure of the range change at sparse locations within the interferogram [see (3)]. The GPS observations are not expected to have significant systematic errors. Therefore, we can use the differences between the interferometric and scaled GPS-measured slant–range shift, at the sparse GPS locations, for a least squares (LS) estimation of the residual phase plane. The estimated phase plane is then eliminated from the interferogram (tilting). Result of tilting the interferogram in Fig. 2(e) is shown in Fig. 2(f).

C. Estimation of Tilting Errors

An interferogram can be correctly tilted with aid of three separately located GPS observations as long as both the complementary interferometric and GPS datasets are error free and describe exactly the same motions. This is not the case for real data. We have found the discrepancy of the complementary datasets from the Reykjanes Peninsula to be mainly due to random noise errors. Thus, the accuracy of tilting is expected to increase with increased number of GPS observations and also with more randomly located GPS points and more coverage of the total image area. An estimate of the tilting accuracy with the number of GPS observations is shown in Fig. 2(h). The estimate is obtained by the following.

- 1) Assume the residual phase plane, used to tilt the interferogram in Fig. 2(e), to be correct (phase plane estimated by using all the 34 GPS observations located within the image areas).
- 2) Residual phase planes are then also calculated for the same interferogram by rejecting 1–31 of the 34 GPS observations and by randomly testing different combinations of GPS points for each number of rejected points. By doing this, we gain also an estimate of the possible variation of the accuracy.
- 3) A tilting error is estimated as the absolute value of the maximum difference between the correct phase plane and a phase plane estimated when taking out GPS points.

The scatterplot in Fig. 2(h) shows that the accuracy can highly depend on which of the GPS points are rejected, and the lowest scatter values indicate that it is possible to obtain accurate tilting when taking out up to 31 points. However, the risk of wrong tilting grows highly and gradually with an increased number of rejected points. In Fig. 2(h), a low maximum tilting error within one fringe (2.835 cm) is always obtained when excluding up to 14 GPS points (using 20 points). Our experiments show that the tilting results are visually close to be the same when arbitrarily rejecting 1–14 GPS points. The result in Fig. 2(h) indicates a highly increased risk of wrong tilting when rejecting much more than ~ 25 points (using less than ~ 10 points).

VI. INITIAL CIRCLE NUMBERS

A virtual unwrapped interferogram (\mathbf{i}_V) can be created by interpolating sparsely GPS-measured range change. A number of methods exists for interpolation of sparsely located observations. Here, we use an ordinary kriging algorithm, which has proven to be very efficient for such interpolation [11], [12]. Kriging algorithms use geostatistical measurements to find an optimal set of weights used for the interpolation, calculated from an estimated semivariogram [13], [14]. One advantage of the ordinary kriging algorithm is its simplicity compared to other kriging algorithms.

The GPS observations are scaled to the elapsed interval of the tilted interferogram (\mathbf{i}_W) and a virtual interferogram created from kriging of the scaled GPS-measured range change. The virtual interferogram can be used to estimate an initial circle number matrix as

$$\mathbf{n}_i = (\text{round}) \left(\frac{\mathbf{i}_V - \mathbf{i}_W}{\frac{\lambda}{2}} \right) \quad (7)$$

where the round operator rounds the matrix values to its nearest integer. If \mathbf{n} is taken as the expected (correct) circle number matrix and $\mathbf{i}_{U_w} = \mathbf{i}_W + \mathbf{n}\lambda/2$, then for each pixel k , n_{ik} in (7) is a correct estimation of n_k as long as $i_{V_k} - i_{U_{wk}} \in [-\lambda/4, \lambda/4]$, where $\lambda/4 \approx 14.2$ mm for the ERS satellites.

For the Reykjanes Peninsula, comparisons have shown that the scaling of the observed GPS motion vectors leads to a tolerable fit between most of the 1993–1998 GPS observations and the tilted interferograms that represent various elapsed time intervals between 1992 and 1996. Consistency between the scaled GPS data and the interferograms has been ensured by excluding from the GPS dataset measurements in poor agreement with the tilted interferogram, especially GPS observations that are expected to result in $|i_{V_{k_{\text{GPS}}}} - i_{U_{wk_{\text{GPS}}}}| > \lambda/4$, where k_{GPS} are pixels corresponding to GPS sites (note that $i_{V_{k_{\text{GPS}}}}$ are the sparse GPS observation of the slant–range shift). This gives an idea of the tolerable discrepancy between the GPS and interferometric observations. The number of rejected points does vary between the four interferograms in Fig. 2. We have observed a possible discrepancy to be mainly due to the following:

- 1) GPS points that may fall within areas with time-dependent motions or high errors in the interferometric observations;
- 2) high uncertainties of some of the GPS observations, especially of the vertical GPS component.

Indeed, by using the GPS uncertainties estimated in [9], (3), and $\hat{\mathbf{s}}$ in (4), we calculate the uncertainties in the 1993–1998 GPS observation projected into the slant–range shift as ± 11.3 mm on average. Uncertainties were within ± 13.2 mm at 35 of the GPS sites, but large uncertainty of ± 15.5 mm and ± 19.7 mm were calculated for two of the sites.

Fig. 4 shows the result of estimating an initial circle number matrix for the 4.17-year filtered and tilted interferogram in Fig. 2(f) [the same as in Fig. 4(a)]. It is evident from Figs. 4(d) and 5(b) how effectively the circle number matrix can be initialized by using the virtual interferogram in Fig. 4(b) along with (7). The estimation does, however, result in wrong

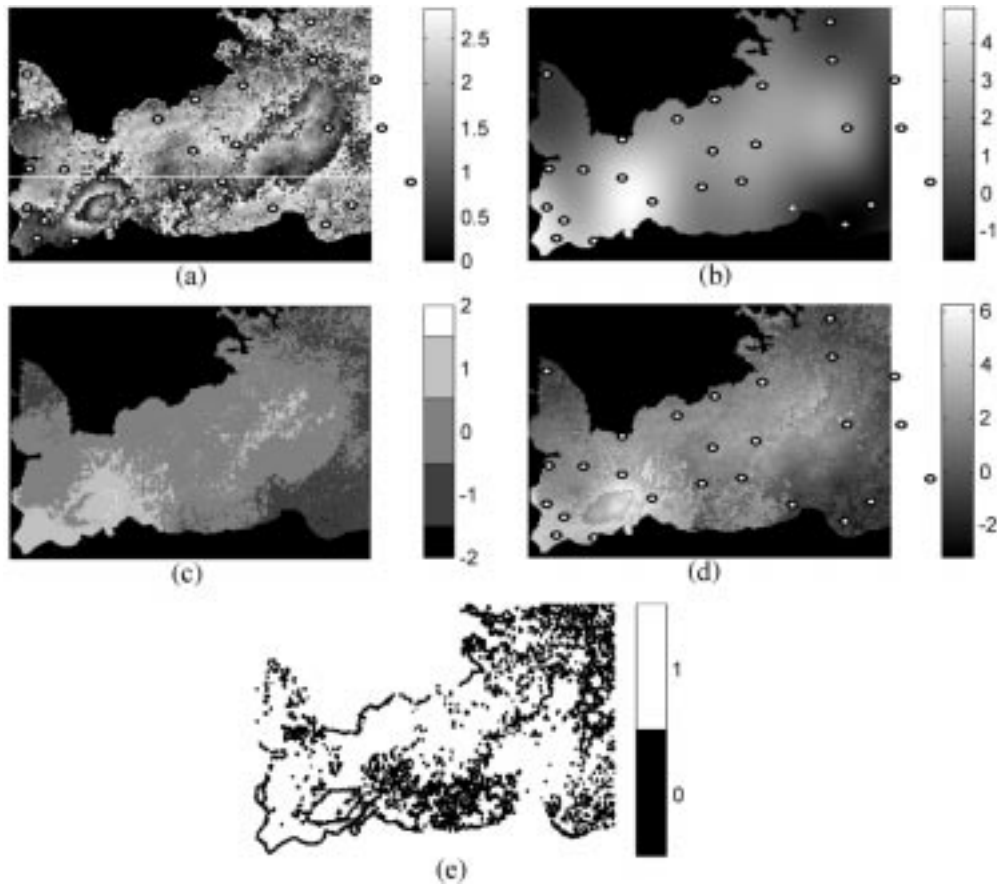


Fig. 4. Estimation of initial circle numbers by aid of GPS observations. (a) 4.17-year wrapped interferogram (i_W). (b) Kriging of scaled GPS-measured slant-range shift (i_V). (c) An initial circle number matrix (\mathbf{n}_i) estimated by (7) with (a) and (b) as an input. (d) Initial interferogram calculated by (1) with (a) and (c) as an input. (e) Mask created for (d) by thresholded edge detection and dilation, where detected areas of interest (areas at and close to sharp edges) are displayed as black color. Sparse locations of GPS observations used to generate i_V are shown as black-and-white circles on (a), (b), and (d). Not all GPS observations, used to create i_V , need to be located within the areas covered by i_V . Here, three of the GPS observations are located outside the image area. The white line in (a) shows the location of the profiles in Figs. 5 and 8.

circle numbers at some image areas. An example is the large time-dependent motions around Svartsengi (subsidence of a circular area; for location see Fig. 1), where the circle numbers are estimated as one number too low.

VII. OPTIMIZATION

A. MRF Regularization and Simulated Annealing Optimization

An MRF model is used to regulate the construction of the circle number matrix \mathbf{n} in (1) [11]. The process is initialized with (7). The regularization is optimized with a simulated annealing iteration process. In the MRF regularization, the optimal matrix (image) \mathbf{n} is interpreted as a realization of a random variable \mathbf{N} . Here, a maximum *a posteriori* (MAP) estimate is used to represent an optimal realization image \mathbf{n} for a given image \mathbf{y} [5], [6], where \mathbf{y} is related to observations. The MAP estimation is given as

$$\hat{\mathbf{n}} = \arg \max_{\mathbf{n}} P(\mathbf{N} = \mathbf{n} | \mathbf{Y} = \mathbf{y}). \quad (8)$$

For convenience, $P(\mathbf{N} = \mathbf{n})$ will be written as $P(\mathbf{n})$ when expressing the likelihood. The Bayesian theorem [15] gives

$$P(\mathbf{n} | \mathbf{y}) = \frac{P(\mathbf{n})P(\mathbf{y} | \mathbf{n})}{P(\mathbf{y})} \propto P(\mathbf{n})P(\mathbf{y} | \mathbf{n}) \quad (9)$$

where $P(\mathbf{n})$ represent a prior expectation about the random field \mathbf{N} (often smoothness assumption), and $P(\mathbf{y} | \mathbf{n})$ is the likelihood of the image \mathbf{y} given the image \mathbf{n} (the relation to the observations).

A very important property of an MRF is that it is defined with respect to its neighborhood system [5], [6], such that a pixel value on an image grid is assumed to be conditionally dependent on its neighborhood pixels only. This is the Markov property, which gives a local definition of the random field. The Markov property is utilized when simulated annealing is used to optimize the MRF regularization, which results in a numerically convenient and less computationally intensive optimization process (see Section VII-C). By using the Hammerley-Clifford theorem [5], [6], [16], the density function in (9) can be written as the Gibbs random field

$$\begin{aligned} P(\mathbf{n} | \mathbf{y}) &= P_T(\mathbf{n} | \mathbf{y}) \propto \exp\left(-\frac{1}{T}U(\mathbf{n} | \mathbf{y})\right) \\ &= \exp\left(-\frac{1}{T}U_1(\mathbf{n})\right) \exp\left(-\frac{1}{T}U_2(\mathbf{y} | \mathbf{n})\right) \\ &= \exp\left(-\frac{1}{T}U_1(\mathbf{n}) + U_2(\mathbf{y} | \mathbf{n})\right) \end{aligned} \quad (10)$$

where $U(\mathbf{n} | \mathbf{y})$ is an energy function defined with both respect to the neighborhood structure of the interferogram [i.e., $U_1(\mathbf{n})$],

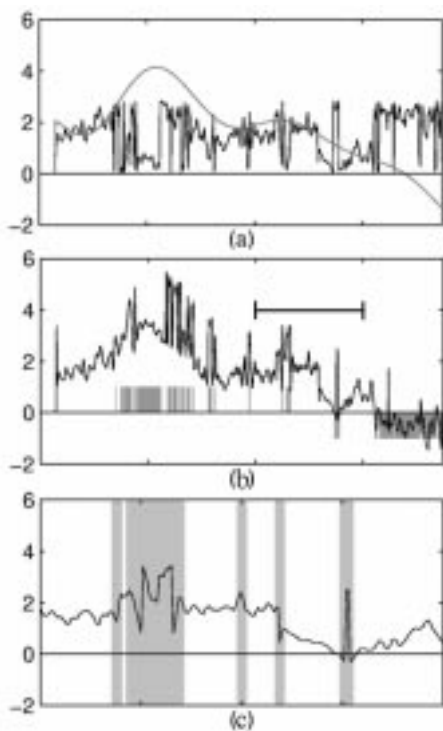


Fig. 5. Profiles from Fig. 4 [see the profile location in Fig. 4(a)]. (a) Profiles from Fig. 4(a) (black line) and Fig. 4(b) (gray line). (b) Profiles from Fig. 4(c) (values are expressed as shaded regions) and Fig. 4(d) (black line). (c) Expanded subsection of the black line in (b), [location labeled with horizontal bar in frame (b)]. The same profile subsection from Fig. 4(e) is also shown in (c), where the location of the shaded regions corresponds to the detected areas of interest (areas at and close to sharp edges), displayed as black colors in Fig. 4(e).

and the relationship of \mathbf{n} to the image \mathbf{y} [i.e., $U_2(\mathbf{y}|\mathbf{n})$], and T is a temperature. The Hammersley–Clifford theorem gives a global definition of the random field, and hence, the MRF modeling can be regarded as defining a suitable energy function

$$U(\mathbf{n}|\mathbf{y}) = U_1(\mathbf{n}) + U_2(\mathbf{y}|\mathbf{n}) \quad (11)$$

that takes its minimum energy stage for the optimal realization image (the unwrapped interferogram).

As $T \rightarrow \infty$, the distribution in (10) becomes uniform among all possible energy states, and as $T \rightarrow 0$, the distribution becomes uniform among the minimum energy states. The simulated annealing optimization can be described as a sampling of the density in (10), where the temperature T starts at some “high” value $T_0 > 0$ and falls toward 0 during the iteration steps. If the temperature is lowered slowly enough, then (10) will assign the maximum probability to the MAP image [17]. One of the great advantages of using the simulated annealing optimization process is its relatively low risk of running into a local minima compared to other optimization algorithms.

B. Smoothness Requirement

Our results have shown that the interferograms from the Reykjanes Peninsula can be unwrapped by only using the smoothness requirements $U_1(\mathbf{n})$ in (11) with $U_2(\mathbf{y}|\mathbf{n}) = 0$, as long as the smoothness of the motion field and speckle noise distortions are within certain limits. Several energy functions were tested that require the surface of the unwrapped interferogram to be smooth.

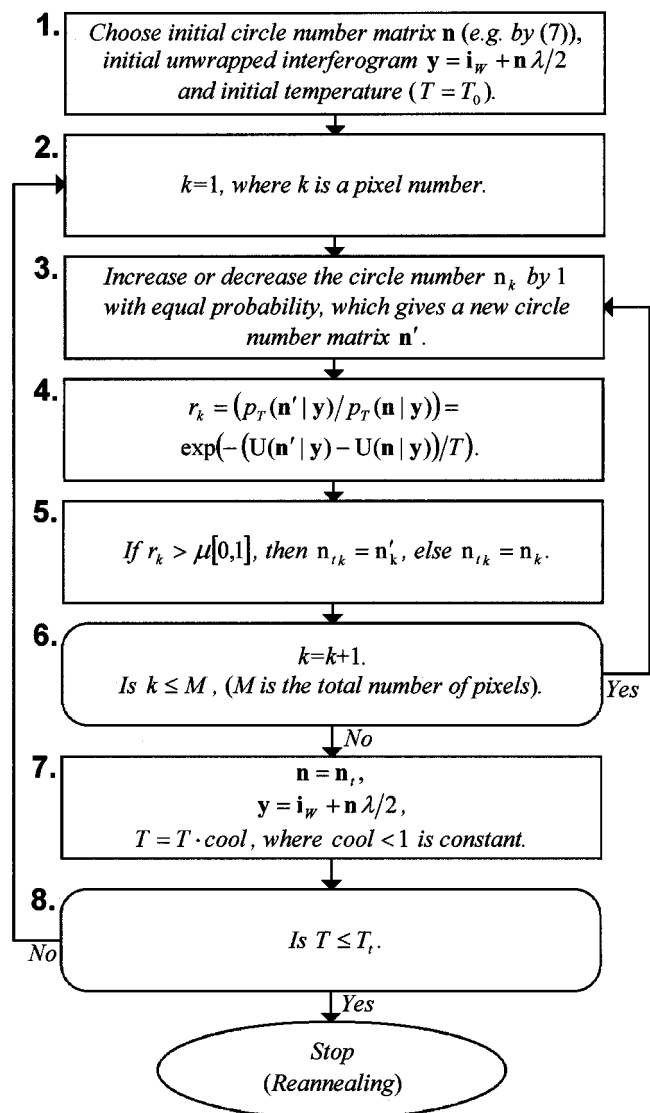


Fig. 6. Block diagram of the simulated annealing algorithm. $\mu[0,1]$ is a random number ranging from 0 to 1, selected from a uniform random generator. The *cool* parameter establishes the temperature fall, and T_t is a “low” temperature used to terminate the algorithm.

The best results have been achieved by requiring smoothness of the first derivative, implemented as a penalization on the second derivative [6] with the approximation

$$U_1(\mathbf{n}) = \gamma_1 \sum_{i \in u} \sum_{j \in v} (f_{i+1,j} + f_{i-1,j} - 4f_{i,j} + f_{i,j+1} + f_{i,j-1})^2 \quad (12)$$

where γ_1 is a constant; u and v are the row and column space, respectively, and $f_{i,j} = i_{w,i,j} + n_{i,j}\lambda/2$.

C. Simulated Annealing Algorithm

The simulated annealing process used for the optimization of (11) is given in Fig. 6. The algorithm uses a nonrecursive update of the pixel values [11]. The MRF regularization favors low-energy states by associating them with high probabilities. The Markov property of the random field is utilized when calculating the ratio of the image probability states with and without

an updated pixel value in Step 4. Because of the Markov property, all terms in the probability formulation not directly related to the pixel under consideration disappear. This is evident by implementing, for example, (12) into the calculation of the image probability ratio in Step 4, i.e., all terms in the summation not directly related to the updated pixel value cancel out in the probability ratio. The algorithm chooses a new energy stage if the probability ratio in Step 5 is larger than a random number within the $[0, 1]$ interval. This allows the algorithm to explore various combinations of circle numbers and, hence, avoid local minima. As $T \rightarrow 0$, the effects from the random generator vanish.

If the temperature is lowered slowly enough, then (10) will assign the maximum probability state or equivalently minimum energy state of (11) to the annealed image [17]. Experience indicates that a “slow” annealing is needed for the optimization when using (12). To avoid slow annealing, without reducing the probability of finding the global solution, the algorithm in Fig. 6 can be used as follows: T_0 is set to a “high” value in Step 1, and one “fast” annealing is done by Steps 2–8. If $T \leq T_t$, then $T = T_0$, and another annealing (reannealing) is done by Steps 2–8. This reannealing process is then repeated until the global solution is found.

D. Guiding With GPS Observations

The scaled GPS-measured slant–range shift includes information about the unwrapped pixel values at sparse locations, and provides a relationship of the circle numbers to observations. This can be utilized in the reannealing process. The GPS pixels can be assigned as a domain of correct pixels and not updated (kept frozen) in the reannealing process. Here, we use an energy function that penalizes only pixels in the nearest neighborhood of the domain of correct pixels with

$$\begin{aligned}
 U_2(\mathbf{y}|\mathbf{n}) = & \gamma_2 \sum_{i \in u} \sum_{j \in v} ((f_{i,j} - f_{i-1,j})^2 W_{i-1,j} \\
 & + (f_{i,j} - f_{i+1,j})^2 W_{i+1,j} \\
 & + (f_{i,j} - f_{i,j-1})^2 W_{i,j-1} \\
 & + (f_{i,j} - f_{i,j+1})^2 W_{i,j+1}) \quad (13)
 \end{aligned}$$

where γ_2 is constant, and the mask \mathbf{W} is 1 within the domain of correct pixels and 0 otherwise. The domain of correct pixels is then expanded before each reannealing with dilation [18], [19, pp. 139–157] by using a structured element with four nearest neighborhood pixels and the pixel. Only the GPS pixels used to initialize the circle number matrix (see Section VI) are used in (13), excluding those lying outside the area covered by the interferograms.

E. Limitations and Parameters

Both the U_1 and U_2 constraints include smoothness assumptions. Hence, the MRF regularization is much more sensitive to high-frequency distortions than small variation of the γ -coefficients when using U_1 and U_2 . Highly decorrelated areas within interferograms (areas with high speckle noise) and sharp edges that are not due to phase cycle boundaries (changes from 0 to 2π or vice versa in phase cycles) decrease the effectiveness of using U_1 and U_2 . High phase gradients and low coherence can

result in phase gradient errors, as explained in [4]. Furthermore, tropospheric and ionospheric artifacts can smear out phase cycle boundaries. Those effects can lead to failure when using the expansion of the domain of the correct pixel (U_2). The vectorized filter is efficiently used to gain temporarily increased smoothness and coherence and, thus, reduce speckle noise and phase gradient errors (Step 2 in Fig. 3). This highly increases the effectiveness of optimizing U_1 and U_2 . Furthermore, we have noted that this also reduces errors of the unwanted smoothing of phase cycle boundaries.

The relative importance of the energy functions in (12) and (13) in the optimization is set by the ratio of the γ_1 and γ_2 coefficients. However, the coefficients represent combination of both scaling and weighting, and evaluation of them requires trial-and-error testing. We found $\gamma_1 = 2$ in (12) and $\gamma_2 = 70$ in (13) to work well for our data. We use reannealing instead of one slow annealing (see Section VII-C and Fig. 6). When reannealing, the initial temperature T_0 is set to a high value, and repeated fast annealings are used. By various experiments, we found the values $T_0 \in [70, 100]$ to work well when using the fast cooling constant $\text{cool} = 0.99$. The best result was achieved though with $T_0 = 90$. Updates of pixel values are then negligible when $T < 2$; hence, we use the termination constant $T_t = 2$.

F. Extracting Areas of Interest

In our reannealing approach, the optimal solution is not reached until after repetition of several “fast” annealing (repetition of Steps 2–8 in Fig. 6), i.e., the interferogram \mathbf{y} in Step 7 in Fig. 6 moves closer to the optimal unwrapped solution with each reannealing. Our results show that after each reannealing, only circle numbers in the nearest neighborhood of sharp edges of the interferogram \mathbf{y} from the previous annealing, especially those close to phase cycle boundaries, are updated. Thus, only those circle numbers need to be optimized (processed) in each reannealing step. Here, this is utilized to make the algorithm faster. A method we use to find the area of interest (nearest neighborhood pixels of sharp edges and phase cycle boundaries) is as follows.

- 1) A thresholded edge detection is used to find large edges in the interferogram \mathbf{y} in Step 7 (Fig. 6) after each reannealing.
- 2) The edge areas are then expanded by a 5×5 constructive element dilation [18], [19, pp. 139–157] to create a mask for the next annealing.

Only masked pixels (pixels close to sharp edges) that are not within the domain of correct pixels are updated in each annealing and other pixels kept frozen. Several edge detection methods have been tested for this purpose. Good results have been achieved with a simple Prewitt operator [11], [18], which finds the steepest gradient by approximating the first derivative. Fig. 4(e) shows an example of a mask, created from the interferogram in Fig. 4(d). The areas of interest (masked pixels) are located at and close to sharp edges and phase cycle boundaries of the interferogram in Fig. 4(d). This is explained further in Fig. 5(c) to show how the areas of interest enclose sharp edges in the interferogram.

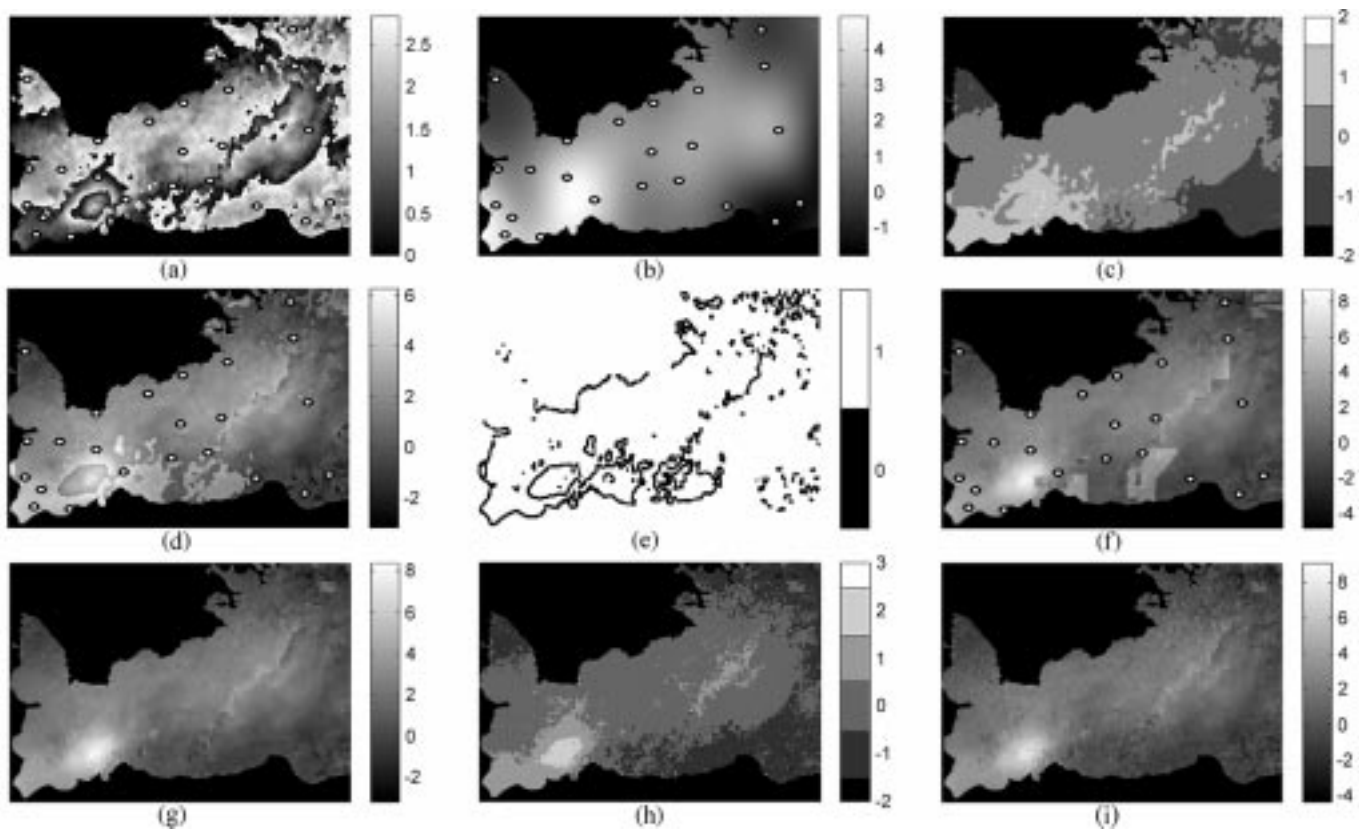


Fig. 7. Demonstration of the unwrapping procedure. (a) Input interferogram [Fig. 2(e)] after tilting and filtering with a $1 \text{ km} \times 1 \text{ km}$ moving-average window. (b) Ordinary kriging of the GPS-measured slant-range shift. (c) Estimated initial circle numbers by using (a) and (b). (d) Part (c) added to part (a). (e) Detected areas of interest (black areas) extracted from (d). (f) Result of simulating annealing optimization after full expansion of the domain of correct pixels. (g) Further optimization of (f) by penalizing only the second derivative [the phase of (g) is congruent with the phase of (a)]. (h) Circle numbers estimated from (g) and Fig. 4(a). (i) Circle numbers in (h) added to Fig. 4(a), giving the unwrapped version of the input interferogram [the phase of (i) is congruent with the phase of Fig. 4(a)]. Sparse locations of GPS points used in (13) are shown as black-and-white circles on some of the subimages.

VIII. RESULTS

A. Unwrapping Process

The methods described so far were used to build up an unwrapping process (see Fig. 3), which was tested on interferograms from the Reykjanes Peninsula in southwest Iceland. The unwrapping process is designed to reduce degradation effects from error factors. The following demonstrates Steps 1–5 in the unwrapping process (Fig. 3) in more detail.

Step 1) The wrapped input interferogram is tilted with aid of GPS observations.

Step 2) The wrapped and tilted interferogram (\mathbf{i}_W) is over-smoothed by vectorized filtering, giving the interferogram \mathbf{i}_{W_s} . This smoothes the surface and makes the optimization of both (12) and (13) easier. Furthermore, this avoids also the errors of unwanted smoothing of phase cycle boundaries, which reduce failures when expanding the domain of correct pixels in (13).

Step 3) Virtual interferogram \mathbf{i}_V is calculated by interpolation (ordinary kriging) of sparsely scaled GPS observations, and an initial circle number matrix (\mathbf{n}_i) is estimated by using (7) with \mathbf{i}_{W_s} and \mathbf{i}_V as inputs.

Step 4) The \mathbf{i}_{W_s} is unwrapped by optimizing (11), where $U_1(\mathbf{n})$ and $U_2(\mathbf{y}|\mathbf{n})$ is given by (12) and (13), respectively. The domain of correct pixels is expanded

before each reannealing, and only pixels within detected areas of interest are updated. After full expansion of the domain of correct pixels, errors are reduced by penalizing only the second derivative, i.e., $U_1(\mathbf{n})$ in (12) with $U_2(\mathbf{y}|\mathbf{n}) = 0$ in (13).

Step 5) The resulting unwrapped interferogram \mathbf{i}_{Uw_s} is used to estimate the circle numbers (integer values) for the input interferogram \mathbf{i}_W by using

$$\mathbf{n}_{Uw} = \text{round} \left(\frac{\mathbf{i}_{Uw_s} - \mathbf{i}_W}{\frac{\lambda}{2}} \right) \quad (14)$$

and an unwrapped version of the tilted input interferogram is then calculated as

$$\mathbf{i}_{Uw} = \mathbf{i}_W + \mathbf{n}_{Uw} \frac{\lambda}{2}. \quad (15)$$

The strategy of using \mathbf{i}_{Uw_s} to estimate \mathbf{n}_{Uw} is the same as using \mathbf{i}_V to estimate \mathbf{n}_i in (7) (see Section VI), except the pixel values of \mathbf{i}_{Uw_s} are closer to the one of \mathbf{i}_{Uw} and, thus, results in much more accurate estimation. Indeed, if \mathbf{n} is the expected (correct) circle number matrix and $\mathbf{i}_{Uw} = \mathbf{i}_W + \mathbf{n}\lambda/2$, then for each pixel k , n_{Uw_k} is a correct estimation of n_k as long as $i_{Uw_s k} - i_{Uw k} \in [-\lambda/4, \lambda/4]$. Thus, n_{Uw_k} is an accurate estimation as long as the oversmoothing results in $< \lambda/4$ deviation of the interferometric values.

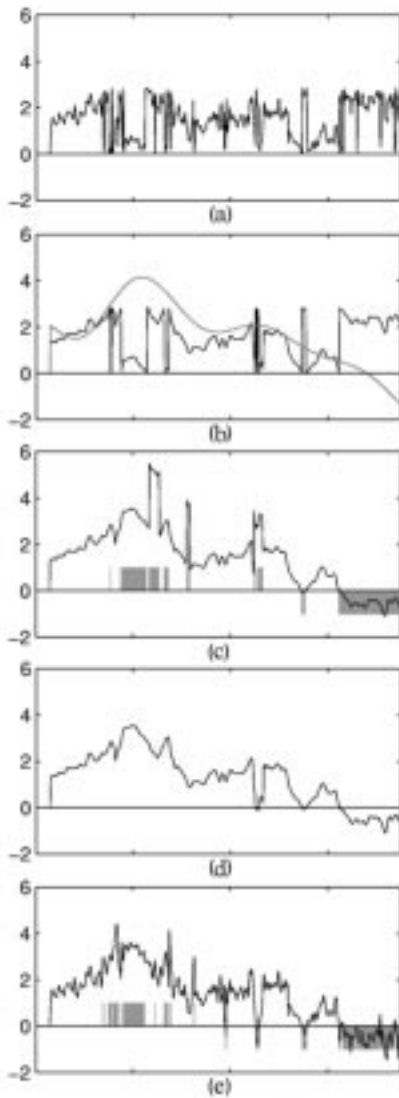


Fig. 8. Profiles from Figs. 4(a) and 7 [see the profile location in Fig. 4(a)]. (a) Profile from Fig. 4(a). (b) Profile from Fig. 7(a) (black line) and Fig. 7(b) (gray line). (c) Profiles from Fig. 7(c) (values are expressed as shaded regions) and Fig. 7(d) (black line). (d) Profile from Fig. 7(g). (e) Profiles from Fig. 7(h) (expressed as shaded regions) and Fig. 7(i) (black line), i.e., the unwrapped version of the wrapped interferogram in Fig. 4(a).

If needed, a 1/0-mask is created with a method described in [11], where only areas with information (e.g., the land areas at the Reykjanes Peninsula) include the value 1. A final interferogram is created by pixelwise multiplication of the resulting unwrapped interferogram and the mask.

B. Unwrapping of the Interferograms From the Reykjanes Peninsula

Steps 2–5 of the unwrapping process (see Fig. 3) are demonstrated in Figs. 7 and 8. The input into the unwrapping process is the 4.17-year interferogram in Fig. 2(e). The result of tilting (Step 1) is shown in Figs. 2(f) and 4(a). The effects of using a vectorized moving-average filter for oversmoothing (Step 2 in Fig. 3) is evident by comparing Fig. 7(a) and (c)–(e) with Fig. 4(a) and (c)–(e), respectively, Fig. 8(a) with Fig. 8(b), and 8(c) with Fig. 5(b). Speckle noise effects and spatial variation have been highly reduced, which, in turn, highly increase the

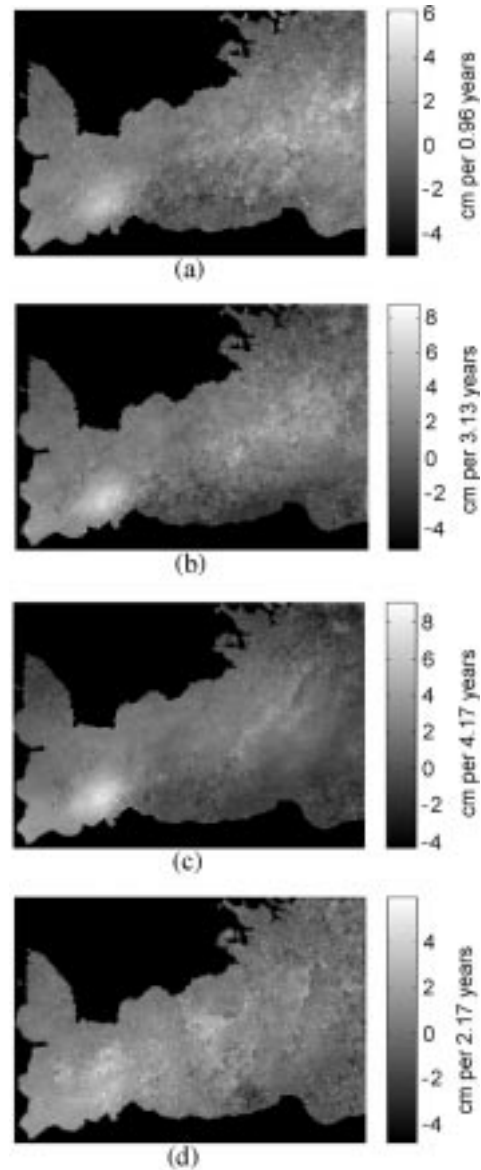


Fig. 9. Unwrapped interferograms from the Reykjanes Peninsula, listed in Table I.

effectiveness of minimizing the energy function (11). Some of unwrapping errors occur when using expansion of the domain of correct pixels [see Fig. 7(f)]. This may be a consequence of unwanted smoothing of phase cycle boundaries or phase gradient errors not successfully eliminated by the vectorized filter. Those errors are reduced by further optimization of the energy function $U_1(\mathbf{n})$ in (12) with $U_2(\mathbf{y}|\mathbf{n}) = 0$ in (13) [Fig. 7(g)]. It is evident from Figs. 7(i) and 8(e) that an accurate estimation of the circle number matrix for the input-wrapped interferogram (\mathbf{i}_W) can be done by using the corresponding oversmoothed unwrapped interferogram (\mathbf{i}_{Uws}) and (14) (Step 5 in Fig. 3). However, the estimation in (14) may result in few pixels or small pixel areas with wrong circle numbers. Such errors are easily reduced by using one annealing or a few more reannealing on the output interferograms (Fig. 3) with Steps 2–8 in Fig. 6 and $U_2(\mathbf{y}|\mathbf{n}) = 0$.

Fig. 9 shows the result of unwrapping the interferograms in Fig. 2. The 4.17-year interferogram in Fig. 9(c) is the same as in

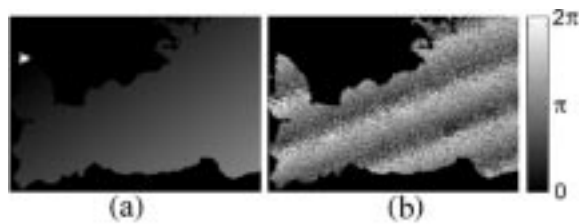


Fig. 10. (a) Phase differences between the tilted and unwrapped interferograms and the wrapped interferograms in Figs. 9(b) and 2(b). (b) Phase differences between the tilted and unwrapped interferograms and the wrapped interferograms in Figs. 9(c) and 2(c). The differences are expressed as a wrapped phase from $0-2\pi$.

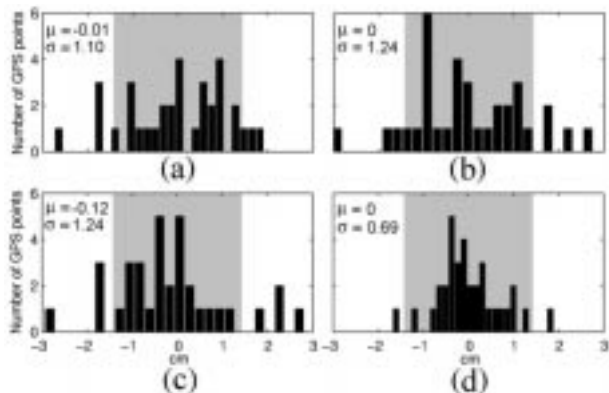


Fig. 11. (a)–(d) Histogram of the difference between the tilted and unwrapped interferograms in Fig. 9(a)–(d), respectively, and the GPS observations of the slant-range shift, scaled to the elapsed intervals of the interferograms. μ and σ are the mean and standard deviation, respectively, of the difference. Shaded regions enclose the interval of $[-\lambda/4, \lambda/4]$, with $\lambda = 5.67$ cm.

Fig. 7(i), i.e., the interferogram was prefiltered before unwrapping. The others were not prefiltered, i.e., they are unwrapped versions of the interferograms in Fig. 2(a), (b), (d).

It is evident from (14) and (15) that all noise errors not eliminated in the input interferogram $\hat{\mathbf{i}}_V$ are inherited in the unwrapped output interferogram $\hat{\mathbf{i}}_{Uw}$. This is reflected in Fig. 10. The phase differences in Fig. 10(a) include only the eliminated phase plane, since the 3.13-year interferogram was not presmoothed. The phase differences between the unwrapped and wrapped 4.17-year interferogram in Figs. 9(c) and 2(c), respectively [see Fig. 10(b)], includes both the eliminated speckle noise (due to presmoothing) and the eliminated phase plane.

The interferograms from the Reykjanes Peninsula are influenced by some tropospheric artifacts (slowly varying structures). This is most evident in the wrapped and unwrapped versions of the 2.17-year interferogram in Figs. 2(d) and 9(d), respectively. Comparison of Figs. 2(a), (b), (d) and 9(a), (b), (d), respectively, and Figs. 2(f) and 9(c) shows how both noise and narrow features are inherited in the unwrapped interferograms.

The consistency between the complementary scaled GPS and tilted interferometric observations from the Reykjanes Peninsula is shown in Fig. 11. The number of inconsistent GPS observations (resulting in $> \lambda/4$ deviation between the complementary datasets) varies from 2–8 points for the four interferograms (lowest and highest for the 2.17- and 4.17-year interferograms, respectively). The results in Fig. 11 indicate high consistency

between the complementary observations, despite of the high errors at some of the GPS sites and some high noise degradation in the interferometric observations. Inconsistent GPS observations can be used, but are best excluded, when estimating initial circle numbers in (7). However, those GPS observations cannot be used in (13), as it will give rise to wrong estimation of circle numbers at and close to them. Here, those GPS sites were excluded in Steps 3 and 4 (see Fig. 3) when unwrapping the interferograms from the Reykjanes Peninsula.

C. Possible Improvements

In our approach (Fig. 3), the oversmoothing in Step 2 reduces the spatial resolution, and hence, it is possible to down-sample after Step 2. The corresponding unwrapped interferogram is then up-sampled again after Step 4, or before estimating the circle number matrix for the tilted “nonsmoothed” input interferogram in Step 5. This has been tested on some of the interferograms from the Reykjanes Peninsula. In those cases, a $1 \text{ km} \times 1 \text{ km}$ moving-average window (10×10 pixel) was used for the oversmoothing. A good result was achieved by down-sampling by a similar amount of pixels, or up to ten pixels in both the azimuth and range. Down-sampling by ten pixels reduces the image size of the interferograms in Fig. 2 from 450×750 to 45×75 pixels. By using a down-sampling, far fewer pixels need to be interpolated in Step 3 and updated in the unwrapping procedure in Step 4. Furthermore, the penalizing of U in (11) becomes more efficient as the distance between highly correlated pixels is shorter. All this makes the unwrapping procedure more effective and much less computationally intensive.

Phase gradients between neighboring pixels in interferograms may exceed one phase cycle (exceed one cycle/sample), e.g., due to low coherence or large observed displacements. This induces phase gradient errors or phase residues [4]. Ignoring such errors can result in underestimation of slopes and wrong estimation of circle numbers. Here, the probabilities of phase residues are highly reduced by the vectorized filtering (Step 2 in Fig. 3). However, the smoothing may not eliminate all such errors, which, in turn, can result in a failure when expanding the domain of correct pixels in (13). Methods exist to locate areas (branch-cuts) where the phase exceeds one cycle/sample [4]. Such methods can be used to extract additional information for the MRF regularization, e.g., to avoid crossing branch-cuts when expanding the domain of correct pixels or to relax the smoothness requirement in (12) of pixels related to branch-cuts.

Various additional prior expectations may exist about the unwrapped phase that can be utilized in the MRF regularization. More prior expectation results in better definition of circle numbers. Such additional knowledge can be incorporated into the MRF regularization by either modifying the constraints in (12) and (13) or adding energy terms to (11). This would require no modification of the simulated annealing algorithm as reflected in Step 4 in Fig. 6.

IX. DISCUSSION AND CONCLUSION

MRF regularization and simulated annealing optimization were incorporated into a procedure for unwrapping interferograms. The technique has been used to unwrap interferograms

with subtle fringe patterns due to deformation of the earth's surface, but not with topographic fringes, as they were removed by use of a DEM when the interferograms were formed. The unwrapped interferograms are a superposition of wrapped interferograms, as well as circle number matrices that are determined by the procedure. Smoothly varying deformation is assumed, implemented as a minimization of the second derivative of the output interferograms. Known 3-D surface displacement vectors from repeated GPS measurements of crustal deformation are incorporated into the procedure as well. The optimal unwrapped interferogram minimizes, then, a set of suitable energy functions that are based on the smoothness assumption and the constraints from the GPS results. The energy functions are designed such that each pixel value in the interferograms is dependent on its nearest neighbor pixel values only, and hence, the interferograms can be treated as an MRF. A simulated annealing algorithm was successfully used to optimize the MRF regularization of the circle number matrices. Due to the MRF property, each pixel in the interferograms can be treated separately and with respect to its nearest neighbors only, which is of great advantage when optimizing the circle number matrices. The procedure was used to unwrap a series of interferograms from southwest Iceland.

ACKNOWLEDGMENT

The authors wish to thank three anonymous reviewers who greatly improved this manuscript.

REFERENCES

- [1] D. Massonnet and K. L. Feigl, "Radar interferometry and its applications to changes in the earth's surface," *Rev. Geophys.*, vol. 36, pp. 441–500, Nov. 1998.
- [2] D. Massonnet, H. Vadon, and M. Rossi, "Reduction of the need for phase unwrapping in radar interferometry," *IEEE Trans. Geosci. Remote Sensing*, vol. 32, pp. 489–497, Mar. 1996.
- [3] A. Leick, *GPS Satellite Surveying*. New York: Wiley, 1990.
- [4] R. Bamler and P. Hartl, "Synthetic aperture radar interferometry," *Inverse Problems*, vol. 14, pp. R1–R54, 1998.
- [5] J. M. Carstensen, "Description and simulation of visual texture," Ph.D. dissertation, Inst. Math. Modeling, Technical Univ. Denmark, Lyngby, Denmark, 1992.
- [6] S. Z. Li, "Markov random field modeling in image analysis," in *Computer Science Workbench*, T. L. Kumii, Ed. New York: Springer-Verlag, 2001.
- [7] R. Hanssen, *Interferometry: Data Interpretation and Error Analysis*. Norwell, MA: Kluwer, 2001.
- [8] S. Hreinsdóttir, "GPS geodetic measurements on the Reykjanes Peninsula, SW Iceland: Crustal deformation from 1993 to 1998," M.S. thesis, Univ. Iceland, Reykjavik, Iceland, 1999.
- [9] S. Hreinsdóttir, P. Einarsson, and F. Sigmundsson, "Crustal deformation at the oblique spreading Reykjanes Peninsula, SW-Iceland: GPS measurements from 1993 to 1998," *J. Geophys.*, vol. 106, pp. 13 803–13 816, 2001.
- [10] H. Vadon and F. Sigmundsson, "Crustal deformation from 1992 to 1995 at the Mid-Atlantic ridge, southwest Iceland, mapped by satellite radar interferometry," *Sci.*, vol. 257, pp. 194–197, Jan. 1997.
- [11] S. Gudmundsson. (2000) Crustal deformation mapped by combined GPS and InSAR. M.S. thesis, Inst. Math. Modeling, Technical Univ. Denmark, Lyngby, Denmark. [Online] http://www.norvol.hi.is/internal_rep.html.

- [12] S. Gudmundsson, F. Sigmundsson, and J. M. Carstensen, "Three-dimensional surface motion maps estimated from combined InSAR and GPS data," *J. Geophys. Res.*, 2001.
- [13] A. G. Journel, "Short course presented at the 28th International Geological Congress," in *Fundamentals of Geostatistics in Five Lessons*, Washington, DC, 1989.
- [14] A. A. Nielsen. (1998) Geostatistik og analyse af spatielle data. Ins. Math. Modeling, Technical Univ. Denmark, Lyngby, Denmark. [Online] <http://www.imm.dtu.dk/~aa/note67153.pdf>.
- [15] S. M. Ross, *Introduction to Probability and Statistic for Engineers and Scientists*. Berkeley, CA: Univ. California Press, 1987, pp. 20–20.
- [16] J. Besag, "Spatial interaction and the statistical analysis of lattice systems," *J. R. Stat. Soc.*, vol. 36, pp. 192–236, 1974.
- [17] S. Geman and D. Geman, "Stochastic relaxation, Gibbs distributions and the bayesian restoration of images," *IEEE Trans. Pattern Anal. Machine Intell.*, vol. PAMI-6, pp. 721–741, 1984.
- [18] R. C. Conzales and R. E. Woods, *Digital Image Processing*. Reading, MA: Addison-Wesley, 1993.
- [19] J. M. Carstensen, *Digital Image Processing*, 3rd ed, J. M. Carstensen, Ed. Lyngby, Denmark: Inst. Math. Modeling, Technical Univ. Denmark, 1998.



Sverrir Gudmundsson received the C.S. degree in engineering from the University of Iceland, Reykjavik, in 1995, and the M.S. degree in engineering from the Technical University of Denmark, Lyngby, in 2000.

He joined the Science Institute, University of Iceland in 1995, as Technical and Research Engineer. He was then with the Nordic Volcanological Institute, Reykjavik, from 1999 to 2000. He rejoined the Science Institute, University of Iceland in 2000. His current work includes claimed, mass-, and energy balance, and iceflow model research at Icelandic glaciers, and the application of remote sensing for studying deformation of the earth's surface.



Jens Michael Carstensen received the M.S. degree in engineering and the Ph.D. degree in statistical image analysis, both from the Technical University of Denmark, Lyngby, in 1988 and 1992, respectively.

He joined the Technical University of Denmark faculty in 1992 as Assistant Research Professor and is currently Associate Professor of statistical image analysis. His current research interests include statistical methods for image analysis, Markov random fields, texture analysis, shape and appearance models, and industrial and biotechnological applications.



Freysteinn Sigmundsson received the M.S. degree in geophysics from the University of Iceland, Reykjavik, in 1990, and the Ph.D. degree in geophysics from the University of Colorado, Boulder, in 1992.

He joined the Nordic Volcanological Institute, Reykjavik, Iceland, in 1992 as a Research Geophysicist and is currently Director of the Institute. His research interests include the dynamics of volcanoes, as well as processes responsible for deformation of the earth's surface.